Global-scale electron precipitation features seen in UV and X rays during substorms

N. Østgaard,[1] J. Stadsnes,[1] and J. Bjordal[1]

R. R. Vondrak[2] and S. A Cummer[2]

D. L. Chenette[3]

G. K. Parks[4] and M. J. Brittnacher[4]

D. L. McKenzie[5]

Abstract. The Polar Ionospheric X-ray Imaging Experiment (PIXIE) and the ultraviolet imager (UVI) onboard the Polar satellite have provided the first simultaneous global-scale views of the patterns of electron precipitation through imaging of the atmospheric X-ray bremsstrahlung and the auroral ultraviolet (UV) emissions. While the UV images respond to the total electron energy flux, which is usually dominated by electron energies below 10 keV, the PIXIE, 9.9-19.7 keV X-ray images used in this study respond only to electrons of energy above 10 keV. Previous studies by ground-based, balloon, and space observations have indicated that the patterns of energetic electron precipitation differ significantly from those found in the visible and the UV auroral oval. Because of the lack of global imaging of the energetic electron precipitation, one has not been able to establish a complete picture. In this study the development of the electron precipitation during the different phases of magnetospheric substorms is examined. Comparisons are made between the precipitation patterns of the high-energy (PIXIE) and low-energy (UVI) electron populations, correlated with ground-based observations and geosynchronous satellite data. We focus on one specific common feature in the energetic precipitation seen in almost every isolated substorm observed by PIXIE during 1996 and which differs significantly from what is seen in the UV images. Delayed relative to substorm onsets, we observe a localized maximum of X-ray emission at 5-9 magnetic local time. By identifying the location of the injection region and determining the substorm onset time it is found that this maximum most probably is caused by electrons injected in the midnight sector drifting (i.e., gradient and curvature drift) into a region in the dawnside magnetosphere where some mechanism effectively scatters the electrons into the loss cone.

1. Introduction

The International Solar Terrestrial Program, ISTP, provides a unique opportunity to study the global substorm. Combining satellite monitoring, ground-based measurements, and remote-sensing techniques such as visible, UV, and X-ray imaging, one might be able to establish a comprehensive picture of the substorm development in the entire energy range of precipitating electrons taking part in the global substorm [*Robinson and Vondrak*, 1994]. The first global schematics of the auroral substorm were based on statistical studies of data from a large number of all-sky stations [*Akasofu*, 1964, 1968; *Feldstein and Starkov*, 1967]. Many of the large-scale features from these schematics have been confirmed by global UV imagers and visible imagers. As UV and visible emissions are proportional to the total electron energy flux, which is usually dominated by electron energies below 10 keV, the global UV and visible images mainly display the patterns of the low-energy electron precipitation. Visible imagers are also restricted to imaging only the nightside aurora because of contamination by sunlight.

Until recently, global imaging of the energetic electron precipitation has not been available. Our knowledge of this part of the substorm has been based on measurements of cosmic radio noise absorption (riometer) [*Hartz and Brice*, 1967; *Jelly and Brice*, 1967; *Berkey et al.*, 1974], X-ray measurements from balloon campaigns [*Bjordal et al.*, 1971; *Sletten et al.*, 1971; *Kangas et al.*, 1975], particle measurements in space [*McDiarmid et al.*, 1975; *Hardy et al.*, 1985] and X-ray measurements from low-altitude satellites [*Imhof et al.*, 1980; *Chenette et al.*, 1992]. The Polar Ionospheric X-ray Imaging Experiment (PIXIE) is the first true two-dimensional imaging instrument developed to measure the global X-ray emission. As the X rays are produced by high-energy electrons interacting with the contents of the ionosphere, PIXIE provides the ability to study both the spatial and temporal patterns of the global energetic electron precipitation during substorms.

Following the traditional auroral substorm scenario observed by UV imagers [*Elphinstone et al.*, 1996], prior to the substorm onset, there is a growth phase [*McPherron*, 1972]. This is associated with the merging of the interplanetary magnetic field (IMF) at the subsolar magnetosphere due to the southward turning of the IMF, accomplishing a more efficient coupling and energy transport from the solar wind into the magnetosphere. During the growth phase, auroral signatures of directly driven dayside precipitation [*Feldstein and Starkov*, 1967; *Vorobjev et al.*, 1976; *Elphinstone et al.*, 1991; *Sandholt et al.*, 1998] and transpolar arcs [*Elphinstone et al.*, 1996] can be seen. These patterns, sometimes called precursors, may develop dawnward or duskward as the

---

[1]Department of Physics, University of Bergen, Bergen, Norway.

[2]Laboratory for Extraterrestrial Physics, Goddard Space Flight Center, Greenbelt, Maryland.

[3]Lockheed-Martin Advanced Technology Center, Palo Alto, California.

[4]Geophysics Program, University of Washington, Seattle.

[5]The Aerospace Corporation, Los Angeles, California.

merging of the field lines propagates into the nightside magneto-sphere [*Elphinstone et al.*, 1991]. As the growth phase signatures seen at the dayside, dawnside, and duskside are usually related to soft electron precipitation, such precursors can hardly be seen in the measurements of the energetic precipitation. However, the arc brightening in the midnight sector, probably due to the stretching of the tail and the subsequent scattering of energetic particles because of the critical relation between gyroradius and magnetic curvature radius [*Sergeev et al.*, 1983], should be observable [*Pytte and Trefall*, 1972].

The substorm onset is believed to initiate at the equatorward edge of the diffuse nightside aurora with a source region at the inner edge of the central plasma sheet (5-7 R_E) [e.g., *Friedel et al.*, 1996; *Elphinstone et al.*, 1996; *Sergeev et al.*, 1998] and is seen as a rapid brightening followed by an expansion longitudinally and latitudinally. Injection signatures at geosynchronous satellites are frequently observed simultaneously with the auroral onset [*Erickson et al.*, 1979] and are often used as onset indicators [*Friedel et al.*, 1996]. Magnetic pulsations in the Pi2 range have also been regarded as reliable indicators for substorm onset timing and can be attributed to the information exchange between the active source region in the magnetosphere and the ionosphere [*Rostoker et al.*, 1980]. When injections of energetic electrons are observed, we should expect to observe the substorm onset simultaneously in both X-ray and UV measurements. However, not all substorm onsets are associated with these injection signatures of energetic particles. In a statistical study, *Yeoman et al.* [1994] found that 10% of the substorms showed Pi2 pulsation signatures but no injection signatures at geostationary orbit.

Studying statistically the energetic particle substorm by riometer measurements, *Berkey et al.* [1974] found that on the average, substorms of energetic precipitation initiated close to midnight. The average magnetic latitude was found to be 65°, with the onset slightly decreasing in latitude and magnetic local time (MLT) with increasing *Kp* values.

The azimuthal expansion of the auroral patterns and the energetic precipitation can be related to two different types of movement. The injection region itself expands in the near-Earth magnetosphere both radially and azimuthally. Another expansion is caused by the gradient and curvature drift of energetic electrons into the morning sector. From several statistical studies based on satellite measurements [*McDiarmid et al.*, 1975; *Hardy et al.*, 1985], riometer measurements [*Hartz and Brice*, 1967; *Jelly and Brice*, 1967; *Berkey et al.*, 1974], and global images in UV [*Liou et al.*, 1997] and X rays [*Petrinec et al.*, 1998], there are found to exist two maximum regions of energetic precipitation but three maxima in the softer precipitation (<1 keV). *McDiarmid et al.* [1975] and *Hardy et al.* [1985] studied electron measurements in the energy range from tens of eV up to tens of keV, while *Jelly and Brice* [1967] and *Berkey et al.* [1974] studied absorption of cosmic radio noise, which is sensitive to electrons of energies from 10 to 100 keV. Focusing on the energetic precipitation, all these studies found the first and most intense maximum to be situated around midnight and to be related to the injection of fresh electrons and another maximum to be located between dawn and noon, most probably related to the drifting electrons. However, by focusing on electron precipitation at lower energies (<1 keV), there is found to exist an additional maximum in the postnoon region [*McDiarmid et al.*, 1975; *Liou et al.*, 1997], where an almost complete lack of X-ray emission is observed [*Petrinec et al.*, 1998]. All these studies were based on adding all the observed precipitation during all kinds of geomagnetic activity

and providing no information on the temporal behavior of single substorms. By studying X-ray measurements from balloon campaigns, *Sletten et al.* [1971] investigated 45 substorm events from 1963 to 1964 and found that the X-ray enhancements in the dawn to noon sector were delayed with respect to the magnetic substorm onset, corresponding to the drift of ≈140 keV electrons. In another study based on X-ray measurements from balloon campaigns and absorption of cosmic radio noise, *Kangas et al.* [1975] examined a large number of events and found delay times corresponding to 100-200 keV drifting electrons. *Berkey et al.* [1974] examined the absorption expansion velocities and found that the eastward expansion corresponded to the drift time of ≈100 keV electrons, using calculations by *Roederer* [1970]. They found the westward expansion to occur more sporadically and to have an expansion velocity that was only half of the eastward expansion velocity. However, *Berkey et al.* [1974] noted that they could not identify the injection region precisely because of the lack of stations in some local time sectors, introducing some uncertainties in the calculations of energies of the drifting electrons.

In this paper the first results from a statistical study based on images from PIXIE and the ultraviolet imager (UVI) onboard the Polar satellite combined with geosynchronous satellite data and ground-based measurements are presented. While the UVI responds to the total electron energy flux, which is usually dominated by electron energies below 10 keV, the PIXIE X-ray images used in this study are in the energy range of 9.9-19.7 keV, which are X rays produced by electron energies above 10 keV. Thus the UVI and PIXIE provide images from complementary ranges of electron energies, well suited to examine differences in the low- and high-energy range of electron precipitation. With this ability to follow both the spatial and the temporal development of substorms in a wide energy range we should be able to verify assumptions and suggestions put forward in the works mentioned above and establish a more comprehensive picture of the energetic substorm. The study is based on data from 14 isolated substorms during 1996, when PIXIE was operating during the entire substorm. While investigating the data, we have mainly focused on (1) the timing of the X-ray, UV, and magnetic substorm onsets and their correlation with the injection signatures at geostationary orbit and ground-based magnetic measurements, (2) the eastward development of the X-ray substorm, and (3) the maximum of the energetic precipitation which is observed at 5-9 MLT in all of the X-ray substorms but not in all of the UV substorms. We have examined if this localized maximum of X-ray emission could be related to the drift of electrons. Any other differences between the X-ray and UV measurements are briefly discussed.

2. Instrumentation

The PIXIE camera provides images of the X-ray bremsstrahlung seen during substorms. Even though the probability of generating an X-ray photon from an electron slowing down in the atmosphere increases as a function of the initial electron energy, a 200 keV electron only deposits 0.5% of its energy as X rays [*Berger and Seltzer*, 1972]. Nevertheless, these measurements provide the opportunity to study the global energetic electron precipitation, even in the sunlit area.   The instrument is a pinhole camera with four stacked multiwire proportional counters as detecting elements. Two detectors are in the front chamber, which contains a 1.1 atm Ar/CO_2 mixture, has a 0.1 mm Be entrance window, and is sensitive to X-ray photons from ≈2 to ≈10 keV. The rear chamber, with a 2 atm Xe/CO_2 mixture and a 2 mm Be

September 12, 1996
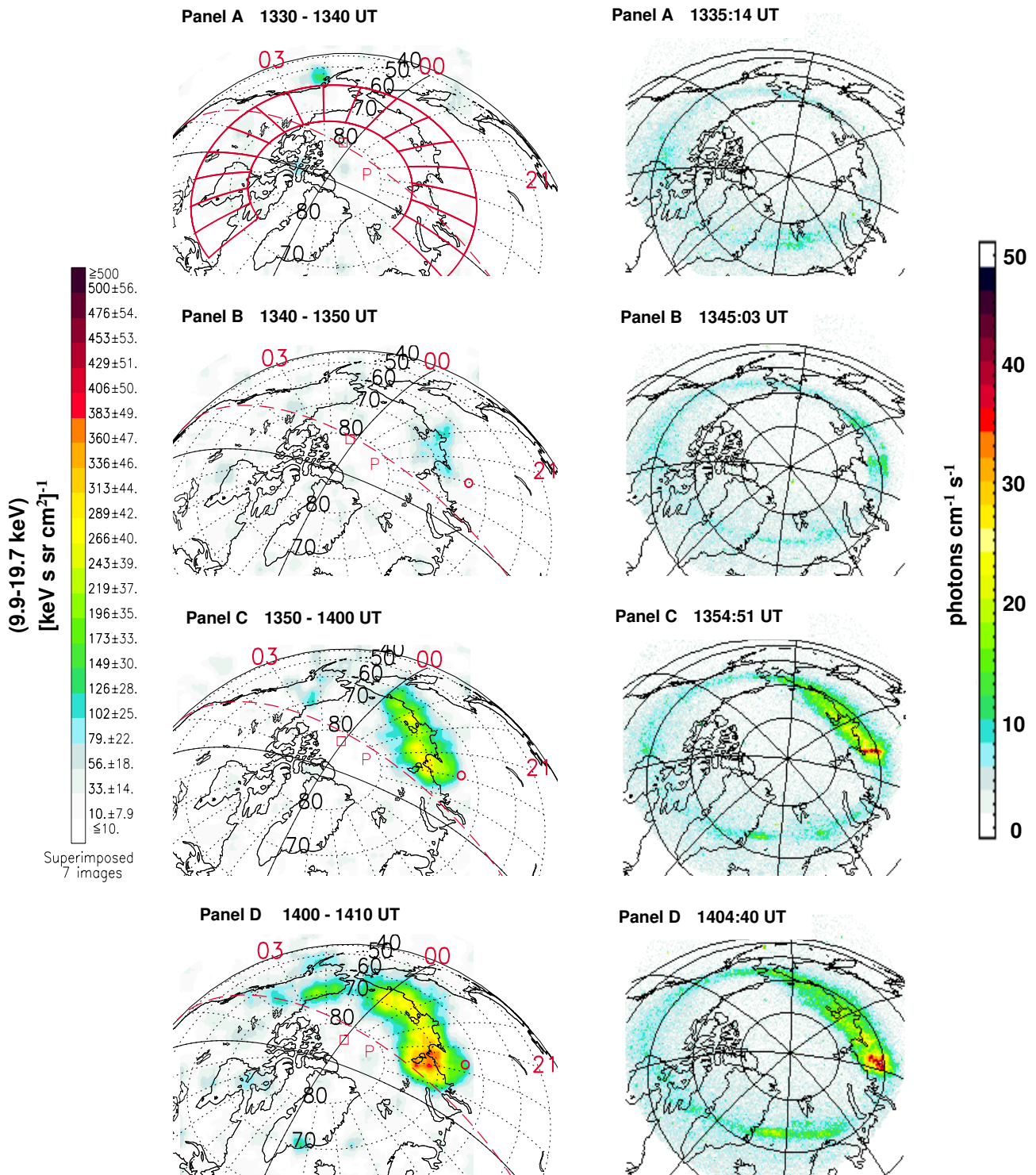
Plate 1. (left) Polar Ionospheric X-ray Imaging Experiment (PIXIE) images, 10 min accumulations in the range 9.9-19.7 keV. The grid is corrected geomagnetic coordinates. (a) The sectors used for calculating the time development of X-ray fluxes are shown. (b)-(e) The location of SC 1994-084 traced into the ionosphere at 100 km height (small red circle) using the Tsyganenko 96 model with solar wind input parameters from the Wind satellite. (right) Ultraviolet imager (UVI) images in the Lyman-Birge-Hopfield-long (LBHL) band. Exposure time is 37 s. The grid is geographic coordinates.
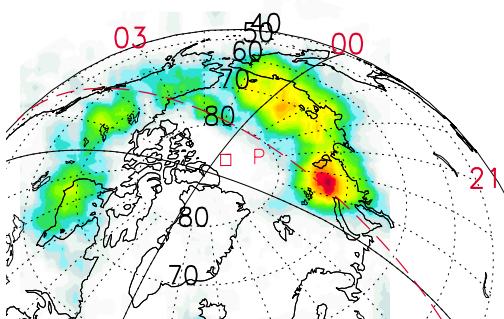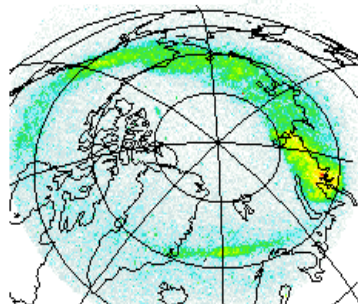
September 12, 1996
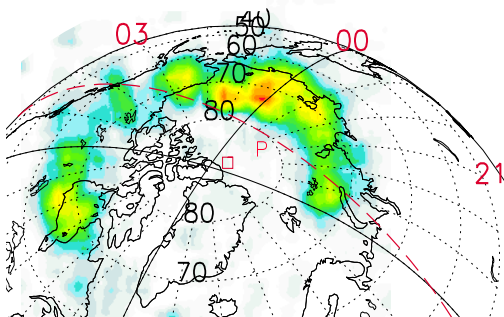
Panel E   1410 - 1420 UT
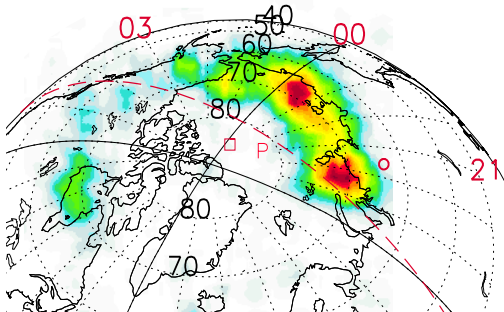
Panel E   1414:29 UT
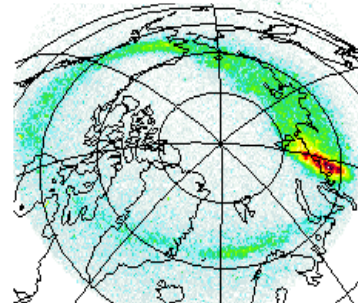
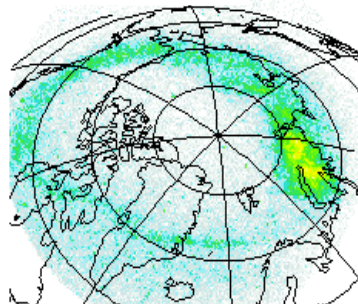**Panel F   1420 - 1430 UT**

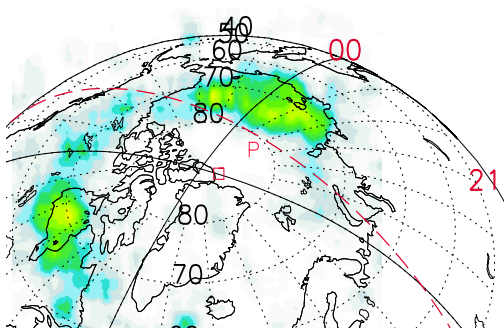**Panel F   1424:18 UT**

Panel G   1430 - 1440 UT

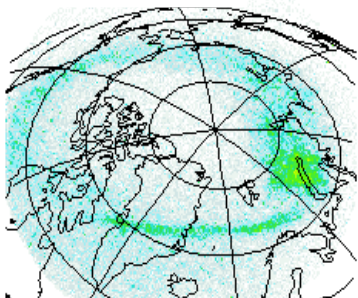**Panel G   1434:07 UT**

Panel H   1440 - 1450 UT

Panel H   1445:09 UT

Plate 1. (Continued)

window, contains the other two detectors and covers the energy range from ≈10 keV to ≈60 keV [*Imhof et al.*, 1995].

As the front chamber was turned off, or partly turned off, during the events of 1996, only X-ray measurements above 9.9 keV were available for this study. As most of the X rays were detected at energies from 9.9 to 19.7 keV, the images shown here are from that energy range. Only electrons above ≈10 keV can produce X rays in this energy range. A background subtraction scheme has been provided by accumulating hours of data when no aurora or celestial sources were seen, giving an average background due to cosmic X rays and X rays produced in the surrounding structures of the instrument by energetic particles. This average background has been subtracted to obtain images of the genuine auroral X rays. The X-ray production layer is assumed to be at 100 km altitude. Each image used in this paper presents 10 min accumulation of the radiation. Images accumulated for 5 min each 30 s are used to present the temporal behavior of the differential X rays integrated in a predefined area, giving a time resolution of ≈30 s.

The UV imager [*Torr et al.*, 1995] onboard the Polar satellite provides global images of emissions in the Lyman-Birge-Hopfield-long (LBHL) band. This band is dominated by the emission created by the electron impact on N_2. All electron energies contribute in this process, and as the absorption of LBHL emissions by atmospheric oxygen is negligible (below ≈10 keV), the intensity reflects the total energy influx of electron precipitation [*Torr et al.*, 1995; *Germany et al.*, 1997]. As the lower energies usually dominate, the UVI provides the global features of the softer part of the electron distribution. The lower threshold energy is determined by the altitude profile of the N_2 versus O density and the upper threshold energy is determined by the decreasing electron flux above 10 keV and the absorption by O_2 at low altitudes. The electron energies, which UVI is sensitive to, are estimated to be from 1 to 10 keV given an energy flux of 1 erg. For larger energy fluxes the threshold may be lowered down to ≈100 eV (G. Germany private communication, 1998). The exposure time for the UVI images shown here is 37 s.

Data from geosynchronous altitude consist of energetic particle measurements from a set of satellites operated by Los Alamos National Laboratory (LANL) and the National Oceanic and Atmospheric Administration (NOAA) Geostationary Operational Environmental Satellite (GOES). All the satellites are used in this study depending on their locations for the different events. As the X-ray emission observed by the PIXIE rear chamber is primarily generated by electrons with energies 10-20 keV, we have mainly focused on the lower-energy channels (50-500 keV) when we compare the ionospheric X-ray fluxes to electron injections seen by the LANL satellites. For comparison between PIXIE and GOES the lowest electron integral channel (>600 keV) is used. As we often observe injections of both electrons and protons during the substorm onset, we have also inspected the injection signatures seen in the proton measurements from the LANL and the GOES spacecrafts. Solar wind data from the Wind satellite and ground-based magnetic measurements from International Monitor for Auroral Geomagnetic Effects (IMAGE), Canadian Auroral Network for the OPEN Program Unified Study (CANOPUS), or Sodankylä have also been studied for each event.

3. Observations and Interpretation.

The images from the PIXIE camera and the UV imager onboard the Polar satellite are the primary data for this statistical substorm study. The Polar satellite was launched February 24,

1996, into a highly elliptical 1.8 x 9 R_E polar orbit with an orbiting period of ≈18 hours. During the apogee passes the imagers are operating for ≈12 hours. To avoid damaging contamination of particles, the PIXIE camera has to be turned off while the satellite passes through the radiation belts. Restricted by this operating time, we have examined the data from 1996 for selecting events where the imagers were operating during the entire substorm event. Only isolated substorms were selected for this study. 14 events from 9 days complied with this requirement. We have chosen the event of September 12, 1996, to present the method used to analyze the entire data set. The results from all the 14 events are listed in Table 1.

3.1. September 12, 1996

The September 12 event occurred during rather disturbed magnetic conditions. A small magnetic storm started on September 10. At 0900 UT on September 12 the *Dst* index was -54 nT, recovering for some hours and showing a new small decrease from -25 to -32 nT around the substorm onset time. The *Kp* index was 4^0. Solar wind parameters from the Wind satellite [9, -21, 2 R_E GSE] were dynamic particle pressure of 5 nPa, proton density of 3 cm^{-3}, solar wind speed of 680 km s^{-1}, interplanetary magnetic field (IMF) B_Z of -4 nT, and IMF B_Y of -2 nT. Plate 1 show 10 min accumulations of PIXIE images in the energy range 9.9-19.7 keV and 37 s exposure of UV images from 1330 to 1450 UT, September 12, 1996.

3.1.1. Growth phase. From the UV images we see growth phase signatures of directly driven precipitation at dawn and dusk from ≈1330 UT (Plates 1a and 1b). These signatures are not seen in the X rays, indicating precursors of mainly soft precipitation.

3.1.2. Onset. From Plates 1b and 1c we see the substorm breakup in the UV. From the intermediate images (not shown) we identify the substorm onset seen in the UV as occurring at 1345:00-1345:30 UT. From Plate 1b we see the X-ray emissions increase around 22 MLT. In Figure 1d the mean differential X-ray fluxes measured by PIXIE in the magnetic sector 21 -22 MLT and 60°-74° corrected geomagnetic (CGM) latitude are shown. The 5 min accumulations of PIXIE images are integrated every 30 s, giving an approximate time resolution of 30 s. We have used the end of the accumulation time interval as the abscissa to determine the enhancement at onset most precisely. From Figure 1 the X-ray onset can be identified at 1345:30 UT in the local time sector from 21 to 22 MLT.

Figures 1a-1c show the particle measurements from two of the LANL satellites. Figure 1a shows the electron measurements from SC 1990-095 located in the noon sector, while Figures 1b and 1c show the proton and the electron measurements at SC 1994-084 located close to the onset source region. An injection of protons at SC 1994-084 is seen about the time of the substorm onset seen in the X rays and the UV emissions (Figure 1b). However, no signature of electron injection is seen, indicating that the electron injection into geosynchronous orbit is taking place eastward of the satellite location at 20.7 MLT. Drift echoes are seen in the electron measurements at SC 1990-095 located in the noon sector. As SC 1994-084 does not see any electron injection during the entire substorm event the source region for the precipitation is probably tailward of the spacecraft. The magnetic footprints of SC 1994-084, shown in Plates 1b-1e, also indicate that the spacecraft is at the earthward edge (southward) of the precipitation area seen by PIXIE and clearly earthward of the UV features during the entire event. However, the spatial resolution in the PIXIE images is not good enough to determine the edge of the precipitating area that
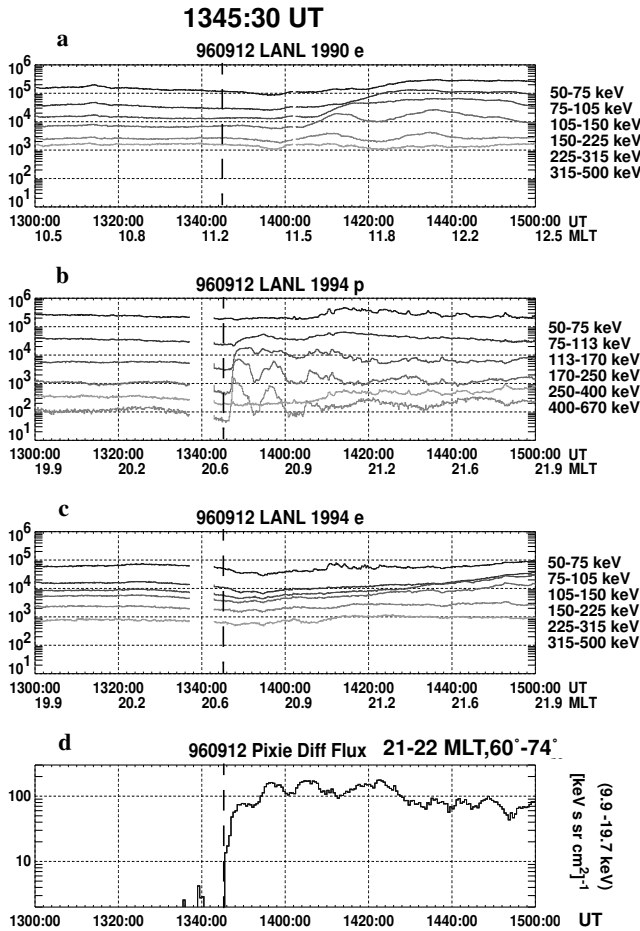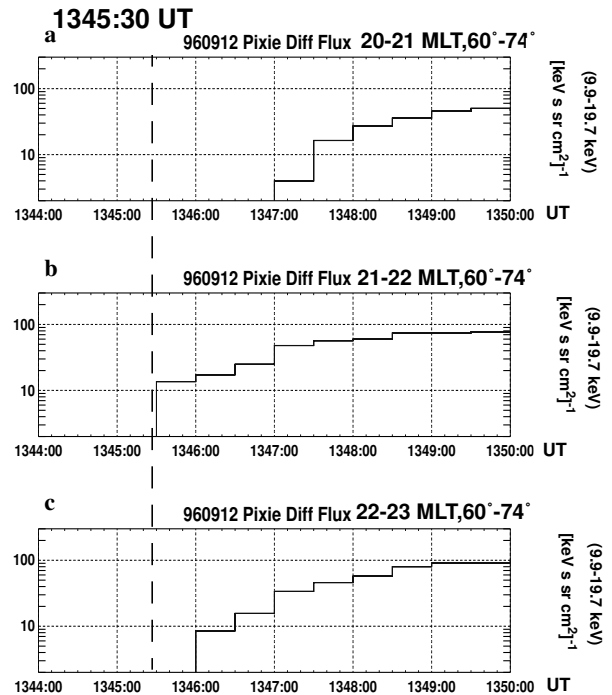
Figure 1. (a)-(c) The particle measurements from the LANL satellites SC 1990-095 (electrons) and SC 1994-084 (protons and electrons). (d) The mean differential X-ray fluxes in the magnetic sector 21 -22 MLT and 60°-74° magnetic latitude. The onset time at 1345:30 UT is marked with a dashed line.

Figure 2. The mean differential X-ray fluxes in the magnetic sectors (a) 20-21 , (b) 21-22 and (c) 22-23 MLT and 60°-74° magnetic latitude. The onset time at 1345:30 UT is marked with a dashed line.

precisely. In Figure 2 the mean X-ray fluxes in three different local time sectors (60°-74° CGM latitude), plotted at a finer timescale, show that the substorm onset takes place in the local time sector 21-22 MLT and expands both eastward and westward into the adjacent sectors.

3.1.3. Expansion phase. In Plates 1c-1e we see from both the PIXIE and the UV images that the injection region expands rapidly eastward and slowly westward. The UV emissions are most intense at the duskward side of the bulge, while the X rays increase significantly eastward, indicating differences in electron energies inside the injection region. From Plates 1f-1g both the UVI and the PIXIE images display features of expansion into the morning sector.

3.1.4. Recovery phase: Maximum precipitation in the morning sector. From ≈1410 UT (Plate 1e) a localized maximum of precipitation is clearly seen in the PIXIE images in the MLT sectors from 6 to 9 at ≈65°-72° CGM latitude, which is not seen by the UVI. As this localized maximum of X-ray emission corresponds to the morning precipitation maximum reported from satellite measurements and cosmic radio noise measurements, we want to examine whether there exists some relation between this maximum and the injected electrons in the onset region. More

specifically, we want to examine whether this localized maximum is caused by electrons injected at midnight during onset, which drifted into the morning sector and scattered into the loss cone by some mechanism. To estimate the time delay of this localized maximum relative to the substorm onset, we have tried to identify the injection front to determine the local time sector of the substorm onset, which can be related to the maximum seen in the morning sector.

In Figure 3 the time development in the 2 hour MLT sectors from 17 to 10 MLT is shown. In the north-south direction all sectors extend from 60° to 74° CGM latitude, as shown in Plate 1a. The 5 min accumulations of X rays sampled every 30 s and a running average of 3 (i.e., 1.5 min) are used. The end of the accumulation time interval is used at the abscissa, giving about a 1 min resolution for the timing of onset but about a 2.5 min too late timing of the maxima (as the center time should be used for the maxima). To improve the statistics, 2 hour MLT sectors were chosen. For fluxes of 250 (keV s sr cm²)⁻¹ the σ is ≈20%, and for 100 (keV s sr cm²)⁻¹ the σ is ≈30%.

For the injection front (20-24 MLT) we identify the onset, the maximum increase rate, and the first significant maximum flux or pulse of injection. We identify the injection region to be the sectors with the largest increase rate of X-ray fluxes, as electrons at all energies are expected to be injected almost simultaneously because of the dipolarization of the magnetic field and the subsequent energization. The adjacent sectors with >70% of the maximum increase rate are interpreted to be within the injection front, as the increase rate of the differential fluxes significantly falls off as the dispersed drift of electron becomes the dominant cause of the eastward movement. Thus, for the event of September 12 the
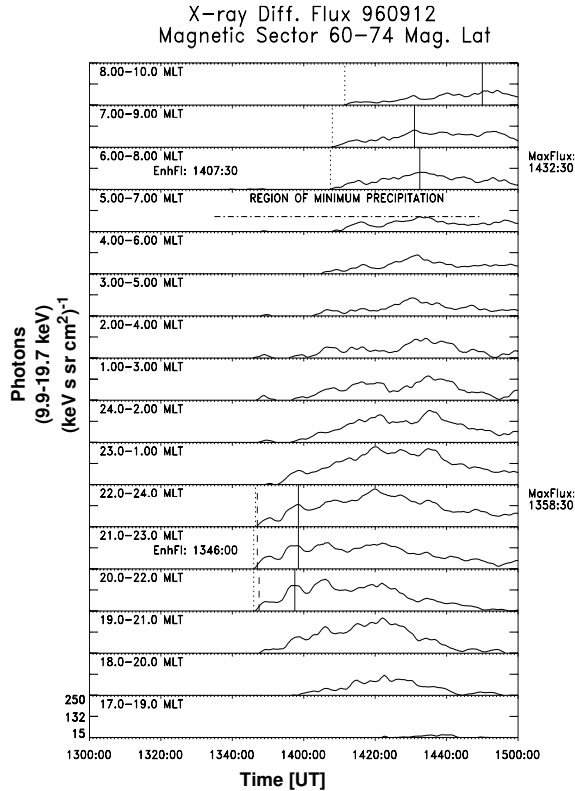
Figure 3. Time development of the mean differential X-ray fluxes in sectors from 17-19 to 8-10 MLT and fixed magnetic latitude 60°-74°. Dotted lines indicate the first enhancement of the mean differential X-ray flux, the dashed line indicates the sectors with the largest increase rate of fluxes and solid lines are the first maxima.

entire injection region is identified to be in the MLT sector from 20 to 24 MLT. The onset is found to occur in the 21-23 MLT sector at 1346:00 UT, and the eastward edge of the injection region is found in the 22-24 MLT sector. This onset time deviates from the onset time found in Figures 1 and 2 because we now use 2 hour sectors instead of 1 hour sectors. The flux decreases in the sectors eastward of the injection region, and the smallest maximum flux is found in the 5-7 MLT sector. Even though the minimum precipitation sector is not very significant for this event, we are able to identify the same intensity (or even a small increase) in the adjacent local time sectors. In the 6-8 MLT sector we identify the first enhancement of precipitation (1407:30 UT), which can be related to the injection sector at 20-24 MLT. This gives us a 21.5 min delay for the onset, 9 sectors eastward of the injection sector. Using a drift model developed by *Lew* [1961], this time delay corresponds to 115 keV electrons. Using a more realistic drift model developed by *Roederer* [1970], the time delay corresponds to 110 keV electrons. From Figure 3 we can see that the first maximum has a larger delay time than the onset (34 min and 8 sectors), corresponding to an electron energy of 65 keV. We may associate the onsets with the first arriving and most energetic electrons and the first maximum with a larger flux of less energetic electrons. In that sense the two time delays (21.5 min and 34 min) display a kind of dispersion signature. To be able to compare the results from the two models, we have calculated the energies for equatorial mirroring electrons. For further information on the drift models see the

appendix.

3.2. The Entire Data Set

Because of the selection criteria mentioned above, we have 14 isolated substorm events available for this study. For each substorm we have identified the substorm onset time from the X-ray and UV measurements, the geosynchronous injection signatures, and the ground-based magnetic disturbances separately. In Table 1 the results from all the 14 substorms are listed.

3.2.1. Growth phase. Growth phase signatures of directly driven precipitation prior to substorm onset are not seen in any of the X-ray substorms but are common features in the UV substorms, confirming that these signatures are mainly caused by soft electron precipitation.

3.2.2. Onset. CANOPUS *AE* indices are used as magnetic onset indicators in the interval from 0200 to 1000 UT and measurements from IMAGE are used for events in the interval 1300-1800 UT. For one event (7: 961210), pulsation measurements from Sodankylä are used to determine substorm onset. From Table 1 we can see that the magnetic, UV, and X-ray substorm onsets tend to occur simultaneously and correlate mostly very well with the injection signatures observed at geostationary orbits. The exceptions are marked with asterisks.

We have UV data for 12 of the 14 substorms. Only one of the UV substorm onset times, i.e., for 961210 (number 7) differs from what we see from the PIXIE images. For this substorm event, which has been thoroughly studied by S. Håland et al. (Magnetospheric and ionospheric response to a substorm: GEOTAIL HEP-LD and Polar PIXIE observations, submitted to *Journal of Geophysical Research*, 1998, hereinafter referred to as Håland et al., submitted manuscript,1998), there are two onsets, one starting at 1704 UT and a second one starting at 1736 UT. The first one is only seen by the UVI, supported by pulsations measurements at Sodankylä, but no injection signatures were seen at geosynchronous orbit. Delayed relative to this first onset there is a transient X-ray enhancement at 1720 UT. The second onset, starting at 1736 UT, is seen in both X rays and UV. Håland et al. (submitted manuscript, 1998) have interpreted the first onset to involve mainly soft electrons, while the second onset includes a broader energy range of electrons.

The magnetic substorm onset defined by the *AE* index correlates very well for 10 of the 14 substorms. In substorm 4 (960920) the onset at 0820 UT is followed by stronger precipitation at 0828 UT. Only the latter precipitation could be seen in the *AE* index from CANOPUS. In substorm 10 (960910) the magnetic substorm starts at 1800 UT while the X-ray substorm, very well correlated with the particle injection seen at geosynchronous orbit, starts at 1809 UT. We have no UV data for this substorm and maybe some soft precipitation, which is not seen by PIXIE, is responsible for the magnetic disturbances prior to this. Substorms 12 (960922) and 14 (960923) occur in Siberia, and the IMAGE stations are probably too far from the onset area to be a good indicator of onset.

Two of the 14 substorms are not seen as injection signatures at geosynchronous orbit. In substorm 5 (960922) the onset at 1132 UT was very weak. A stronger burst of precipitation was seen by both PIXIE and UVI at 1153 UT along with injection signatures seen by one of the GOES at 1157-1202 UT in 3 MLT (i.e., protons drifting in 18 local time sectors). Unfortunately, there was data gap in the LANL electron measurements for this event. In substorm 6 (960923), no injection signatures were seen at 0910 UT, but a larger burst of precipitation correlates very well with the
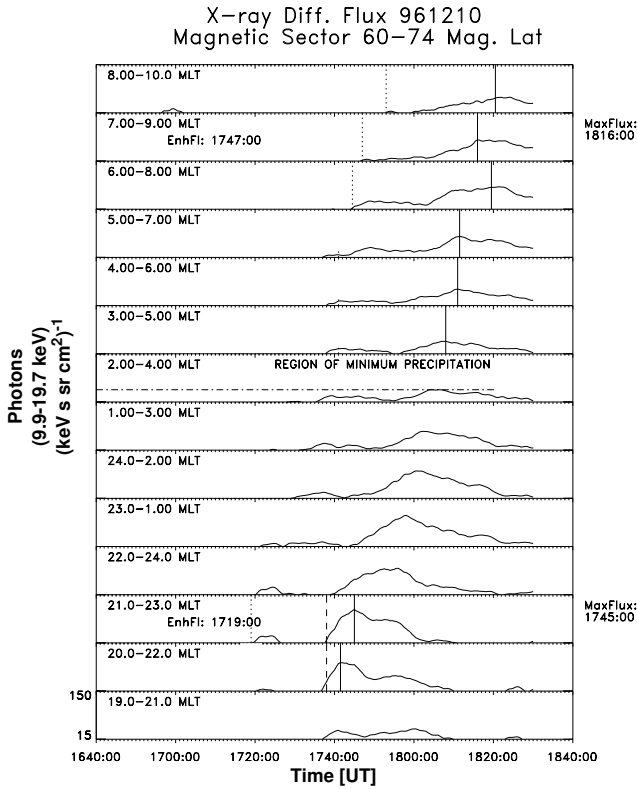
Figure 4. Category 1: one well-defined onset. Dotted, dashed, and solid lines are as in Figure 3.
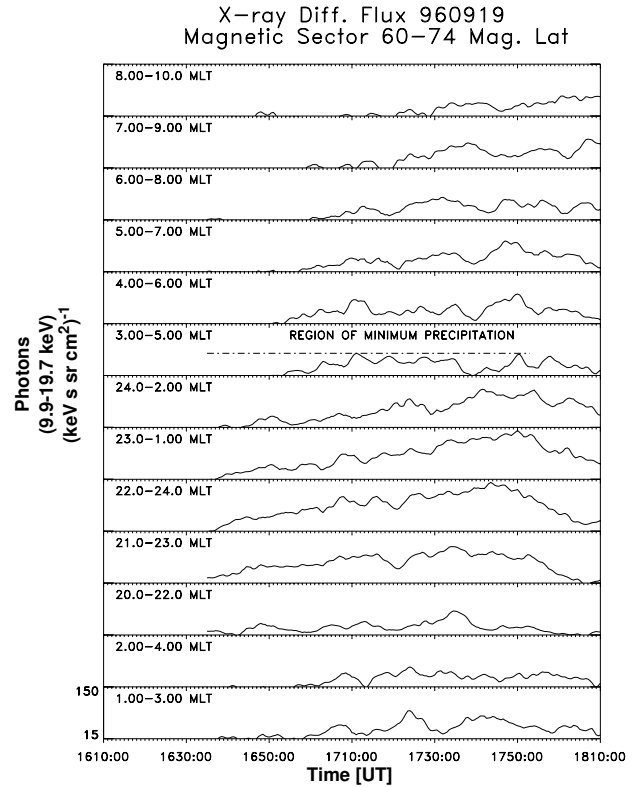
Figure 6. Category 3: onsets or timing of the localized maximum of X-ray emission are not well defined.
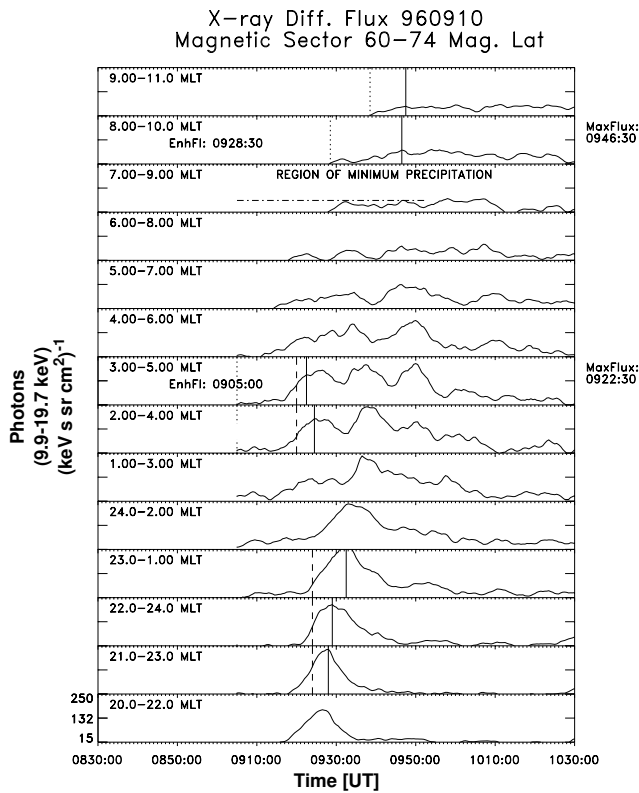
Figure 5. Category 2: two well-defined injection onset regions. Dotted, dashed, and solid lines are as in Figure 3.

injection signature at 0917-0922 UT. For both of these events the injections at substorm onset were probably too weak or the electron energies too low to be detected by the GOES.

3.2.3. Expansion phase. The expansion of the injection region is observed in both X rays and UV. After that, there are significant differences between the UV and X-ray substorms. While the most intense UV emissions tend to persist at the westward edge of the bulge, the X-ray features fade in this region. The energetic precipitation seen as intense X rays tends to move eastward into the morning sector.

3.2.4. Recovery phase: Maximum of X-ray emission in the morning sector. In all of the 14 substorms we observe the maximum of X-ray emission in the morning sector delayed relative to substorm onset. This localized maximum is not seen in any of the UV substorms. To apply the same method as described for the September 12 event and to determine the time delay for the localized enhancement of X-ray emission in the morning sector, we have divided the data set into three subsets.

The first category can be labeled clean events. These have well-defined substorm onset and injection regions, and calculation of the time delay of the maximum in the morning sector is straightforward, as for the September 12 event. One of these events, from December 10, is shown in Figure 4. We identify the injection front to be in the 20-23 MLT sector, and the substorm onset is found in the 21-22 MLT sector. The onset of the morning maximum in the X-ray emission is determined from the 7-9 MLT sector, but can be identified in all the sectors from 3 to 10 MLT.

The second category contains events with more than one substorm onset region. As the substorm onset regions can be identified to determine the corresponding injection onset times, we are

Table 1. Onset Observed As Injections of Electrons (e) or Protons (p) by Geostationary Spacecrafts, Ground-Based Magnetic Measurements, Polar UVI, and PIXIE.

Date	Injection Signatures Geostationary Orbits,[a]		Magnetic Onset,[b]	UV Onset,	X-ray Onset,		Onset of the Localized Maximum of X-ray Emission in the Morning Sector,		Delay Time: Sectors and Corresponding Energies	
	MLT	UT	UT	UT	MLT	UT	MLT	UT	Min : Time Sectors	Lew - Roederer,[c] keV
Well-Defined Onset With One Injection Region and Distinct Timing of the Localized Maximum of X-ray Emission										
1: 960829	G e 2.2	≈0713-0717	C 0713-0715	0715	24	0715	6	0728	13 : 6	130 - 115
2: 960912	L p 20.7	1346	I 1345	1345	22	1346	7	1407:30	21.5 : 9	115 - 110
3: 960920	L e 2.9 (weak)	0526	C 0530	no data	22	0527	5	0549	22 : 7	100 - 80
4: 960920	L p 15.2 L e 5.8	0821 0821	C 0828*	0819	22	0820:30	6	0839:30	19 : 8	115 - 105
5: 960922	G p 3.0	≈1157 - 1202*	I 1130	1131	21	1132	7	1158	26 : 10	105 - 100
6: 960923	G e.0.3 L e 6.8	≈0917-0922* 0921*	C 0915	0910 0919	22	0910	6	0921	11 : 8	200 - 180
7: 961210	L e 1.0 L e 23.0	1704 1737	S 1704 S 1720 S 1737	1704* 1737	22	1720 (1736)	8	1747	27 : 10	100 - 100
Well-Defined Onsets With Two Injection Regions and Distinct Timing of the Localized Maximum of X-ray Emission										
8: 960910	G e 4.0	0908 - 0913	C 0905 C 0918	0905 0918	4	0905	9	0928:30	23.5 : 5	60 - 85
9: 961223	L e 24.0	0236	C 0237	0235	22	0235	6	0259:30	24.5 : 8	90 - 85
Not Well Defined Onsets or Timing of the Localized Maximum of X-ray Emission										
10: 960910	L e+p 1.0	1807	I 1800*	no data	22-23	1809	5-9			
11: 960919	no data	no data	I 1640	1637	23	1636	4-9			
12: 960922	L p 20.3	1324	I 1330*	1323	22	1323	5-9			
13: 960922	L e+p 21.9	1500	I 1500	1500	21	1500	6-10			
14: 960923	L p 17.5	1245	I 1300*	1245	20-21	1246	5-7			

MLT is magnetic local time; UT is universal time; asterisks indicate magnetic, UV, or X-ray substorm onsets that do not correlate well with injection signatures observed at geostationary orbits.

[a]Injections of electrons (e) and protons(p) were observed by the geostationary spacecrafts G, GOES and L, LANL.
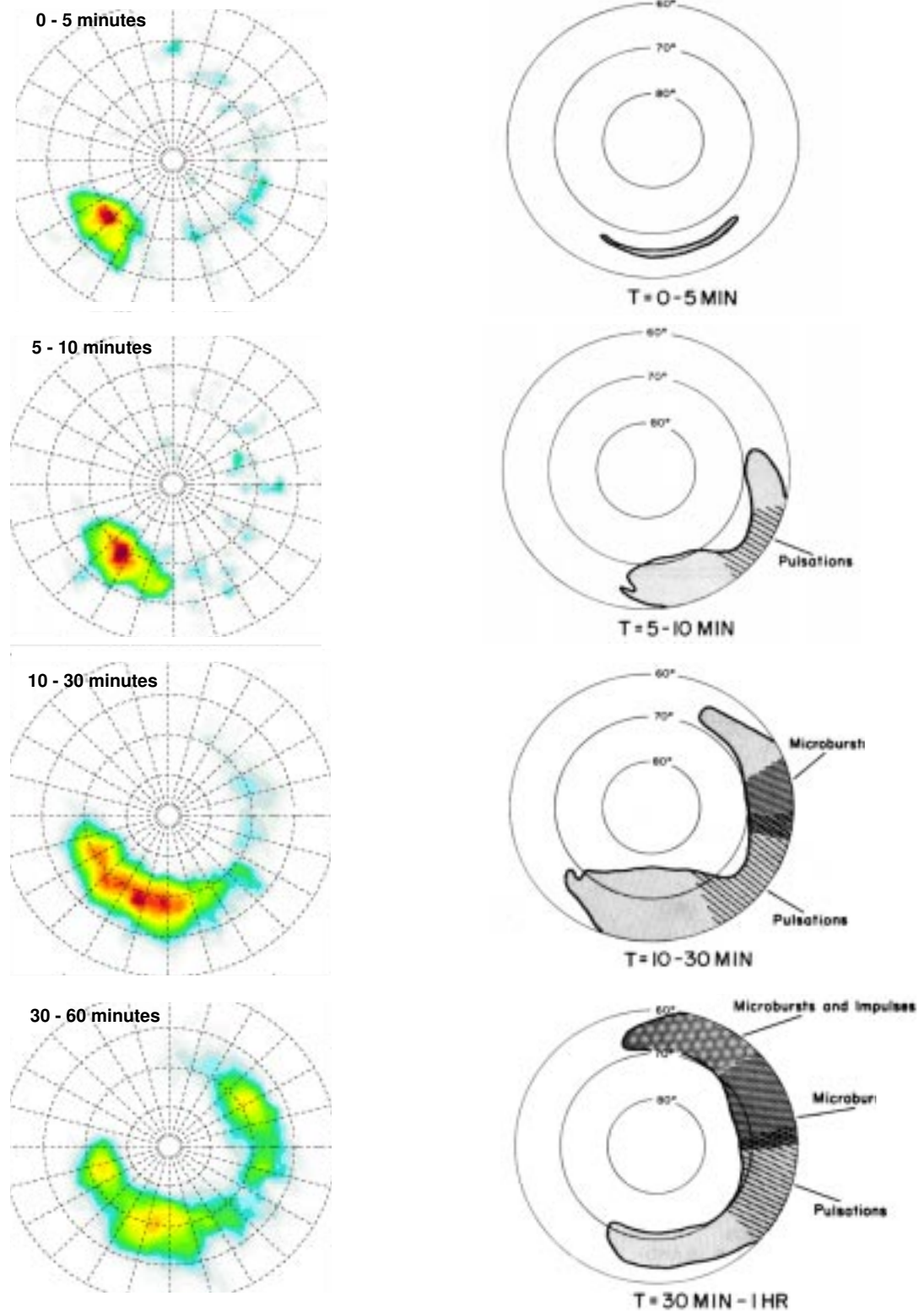
[b]Ground-based magnetic measurements were done by C, Canadian Auroral Network for the OPEN Unified Study (CANOPUS); I, International Monitor for Auroral Geomagnetic Effects (IMAGE); and S, Sodankylä.

[c]Range of delay determined using the methods of *Lew* [1961] and *Roederer* [1970].

still able to find the time delay and calculate the corresponding energy of the drifting electrons. Figure 5 shows such an event from September 10. Similar to the September 12 event, we identify the injection regions to be the sectors with the largest increase rate of X-ray fluxes. For this event we can identify two injection fronts, one covering 2-5 MLT and another covering 21-24 MLT.

Although the maximum in the morning sector is not very pronounced, we are still able to identify an enhancement in the 8-10 MLT sector that exceeds the fluxes in the adjacent sector (7-9 MLT). The injection region and the substorm onset, which can be related to the maximum in the late morning sector (8-10 MLT), are found in the 3-5 MLT sector.

Measured Average X-ray Substorm   **Model [*Akasofu*, 1968]**

0 - 5 minutes

5 - 10 minutes

10 - 30 minutes

30 - 60 minutes

T = 0 - 5 MIN

T = 5 - 10 MIN

T = 10 - 30 MIN

T = 30 MIN - 1 HR

Plate 2. (left) Three single substorms normalized and superimposed. (right) Models by *Akasofu* [1968] based on balloon measurements in the 1960s.

The last category contains events where the maximum in the morning sector is seen, but as it is difficult either to identify the substorm onset region, to distinguish between different onset regions, or to determine the onset in the morning sector, it is impossible to find the time delay and calculate the energy of the drifting electrons. One of these, the September 19 event, is shown in Figure 6. This event has no distinct onset and occurred in the initial phase of a magnetic storm as a response to a coronal mass ejection (CME) event after 1 hour with large southward IMF B_Z.

For the substorms in categories 1 and 2 (10 substorms) we are able to determine onset of the maximum X-ray emission in the morning sector and calculate the electron energies that correspond to the measured time delays. The results are listed in the two rightmost columns of Table 1. The onsets, which may be associated with the first arriving energetic electrons, tend to have a smaller time delay than the first maxima, which may be associated with the larger flux of less energetic electrons. This kind of dispersion signature can be seen in many of the events in categories 1 and 2.

4. Discussion

On the basis of balloon measurements [*Barcus and*

Calculated Energies of Drifting Electrons
Lew [1961]
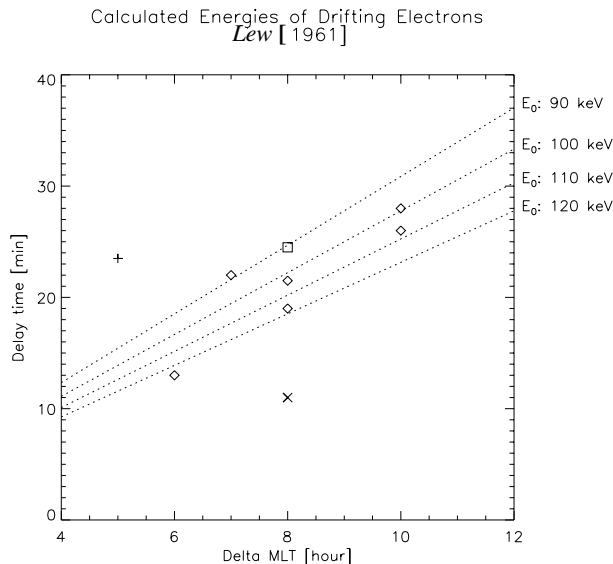
Figure 7. Delay time from substorm onset to onset of the maximum of X-ray emission in the morning sector versus MLT sectors. Substorm onset around midnight ($3 < Kp < 5$) of category 1 (diamonds) and category 2 (squares). The plus is the substorm onset at 4 MLT of category 2 (960910). The cross is the substorm during Kp: 6 - of category 1 (960923). Dotted lines show delay time versus MLT sectors for energies from 90 keV to 120 keV using the drift model of *Lew* [1961].

Rosenberg, 1966; *Parks et al.*, 1968], *Akasofu* [1968] has presented models of what an X-ray substorm would look like. With the global X-ray images provided by PIXIE we should be able to verify his predictions and to develop a more accurate model. Three of the substorms in our data set happen to have substorm onset in the same local time sector. In Plate 2 (left) we have normalized and superimposed these three substorms, representing an average X-ray substorm. The superimposed substorm has to be

rotated 2 MLT sectors counterclockwise to be comparable to the models as all the three superimposed substorms have substorm onset in the 22 MLT sector while the models from *Akasofu* [1968] are based on data with substorm onset close to midnight. Compared to the models by *Akasofu* [1968], we should notice two significant differences. First, the superimposed X-ray substorm does not develop into the morning sector as quickly as was predicted by Akasofu. This can partly be explained by the higher sensitivity to high-energy X rays of the scintillation counters and Geiger-Müller tubes used in the balloon campaigns compared to the proportional counters used in PIXIE. It may also indicate that the electron energies involved in the three superimposed substorms are lower, giving slower drift velocities, than the energies involved in the substorms on which *Akasofu* [1968] based his models. Second, the superimposed X-ray substorm shows a significant morning precipitation maximum during the recovery phase, which is consistent with the statistical studies of *McDiarmid et al.* [1975], *Hardy et al.* [1985], *Hartz and Brice* [1967], and *Jelly and Brice* [1967] and confirm the results from *Berkey et al.* [1974] and *Sletten et al.* [1971], where the morning precipitation maximum was interpreted to be caused by electrons drifting into the morning sector. This maximum is not shown by the *Akasofu* [1968] schematic as the model contains no intensity information.

On the basis of the time delay from substorm onset and onset of the maximum in the morning sector we have calculated the electron energies that correspond to the observed time delays. We have used both a simple dipole drift model by *Lew* [1961] and a more realistic model derived by *Roederer* [1970]. To be able to compare the results from the two models, we have calculated the energies for equatorial mirroring electrons and both models give electron energies around 100 keV. The model of *Roederer* [1970] tends to give 5-20 keV lower energies, but for most of the substorms this discrepancy is smaller than the uncertainties of our determination of time delays. In the appendix the two models are described in more detail. Keeping this in mind, we are able to present the results using the model of *Lew* [1961] in a simple plot, (see Figure 7). For 6 of the substorms in category 1 and one of the substorms in category 2 we have found time delays that correspond to energies in the range of 90-120 keV. For the 960910 event (substorm 8) we find an energy of ≈60 keV. As this substorm onset occurs in 4 MLT and the onset of the maximum is found in 10 MLT, the asymmetry of the magnetic field has to be taken into account, as is done by the model of *Roederer* [1970]. Applying this model, we get an energy of 85 keV. For the 960923 event (substorm 6) the time delay corresponds to 200 keV electrons using *Lew* [1961] and 180 keV electrons using *Roederer* [1970]. This high energy is probably due to the very strong magnetic activity ($Kp = 6-$) during this event. During such disturbed conditions the field deviates strongly from a simple dipole field model. As described in the appendix the model of Roederer needs a constant magnetic contour as an input parameter. The $B_0=100$ nT contour we have used is probably not a good assumption in this case. By letting $B_0=60$ nT the calculated energies decrease with a factor of ≈3/4. (For a more detailed description, see the appendix).

Our results regarding the energies of the drifting electrons are somewhat lower than the results of *Sletten et al.* [1971], ≈140 keV and *Kangas et al.* [1975], 100-200 keV, which may be due to the fact that the detectors used in the balloon campaigns were more sensitive to the (first-arriving) high-energy electrons than the PIXIE camera. However, our results are similar to those found by *Berkey et al.* [1974], ≈100 keV. When *Berkey et al.* [1974] found some very large energies in their study, we think those results

must be explained by the lack of stations in some local time sectors. Consequently, they could have based their calculation on only one injection region when there probably were two or more injections regions in later local time sectors. The electron energies found in this study are more than sufficient to produce the X rays in the energy range of 9.9-19.7 keV. We also want to point out that these energies refer to the first-arriving electrons and that electrons at lower energies probably account for the increasing intensity that constitutes the prolonged localized maximum. By using exponential fit to the electron spectrum measured by the LANL satellites as the source spectrum, calculations based on the method described by *Robinson et al.* [1989] show that the electron fluxes at such high energies are sufficient to produce the observed X rays in the morning sector.

Regarding the location and extension, we find that the morning maximum appears in the local time sector from 5 to 9 MLT. For the substorms in categories 1 and 2 we find about half of the localized maximum of X-ray emission peak intensity to be ≈66°-67° CGM latitude and the other half to be ≈70°-71° CGM latitude. *Newell and Meng* [1994] have examined DMSP satellite measurements during high and low solar wind pressure conditions to determine the ionospheric projection of different magnetospheric regions. Most of our events correspond to their high solar wind pressure conditions ($p > 4$ nPa), and for half of the events the latitudes of the X-ray features correspond to a source region for the localized maximum in the central plasma sheet. For the other half of the events the latitudes of X-ray features correspond to their ionospheric projection of the boundary plasma sheet [*Newell and Meng*, 1994].

At this stage we are not able to explain the mechanism that causes this maximum of precipitation in the morning sector, but we suggest two possible candidates of explanations.

1. One candidate for such a mechanism is the wave-particle interaction of VLF waves and electrons, which has the cold plasma density as an important parameter. This was suggested by *Brice and Lucas*, [1971], *Sletten et al.* [1971], and *Jentsch* [1976]. To trigger this process, an effective diffusion of cold plasma from the sunlit part of the ionosphere is needed to provide the enhancements observed. To relate the drifting electrons to this mechanism, we have to multiply all the energies found in this study by a factor of 1.0-1.5, as we probably have to deal with electrons with pitch angles in the range of 10°-90° rather than equatorial mirroring electrons.

2. Another candidate is more straightforward. Equatorial mirroring energetic electrons injected in the midnight sector from the inner edge of the plasma sheet (5-7 R_E) will drift along contours of constant magnetic magnitude when the influence of the convective electric field can be neglected ($E > ≈100$ keV). These contours are fairly asymmetric [*Fairfield*, 1968] and will cause the electrons to move outward as they drift into the morning sector. During disturbed conditions the magnetosphere is compressed, and the dawn magnetopause could well be at 11-13 R_E, which are the values we get when the solar wind measurements from our data set are used to calculate the dawn magnetopause position, on the basis of the stand-off distance [*Walker and Russell*, 1995] and the relations between the subsolar and the dawn magnetopause [*Sibeck et al.*, 1991]. If this is the case the energetic electrons may drift into the magnetopause. In this region the conservation of the first adiabatic invariant breaks down, and the electrons will be scattered into a fully isotropic distribution. In this case the calculation of energies corresponding to equatorial mirroring electrons

will be valid. For the events where the peak intensity of X-ray emission was found at 66°-67° CGM latitude this explanation is probably not appropriate. However, for the other half, where the peak intensity was found at 70°-71° CGM latitude the source region may be identified closer toward the magnetopause. [*Newell and Meng*, 1994]. Mapping techniques are needed to investigate this hypothesis further.

5. Conclusion

For the first time we have been able to study the global features of the energetic precipitation seen by PIXIE and the softer part of the precipitation seen by UVI simultaneously during isolated substorms. Our main results are as follows.

1. Growth phase signatures of directly driven precipitation at dawn and dusk are not seen by PIXIE but are common features in the UV substorms, indicating mainly soft precipitation.

2. The substorm onsets are seen simultaneously by UVI and PIXIE and correlate very well with injection signatures seen at geosynchronous orbit.

3. During the expansion phase the most intense UV emissions are observed at duskward part of the bulge, while the most intense X rays are moving dawnward.

4. During the recovery phase a maximum of X-ray emission is seen in the morning sector, which confirms the results found by others [*Jelly and Brice*, 1967; *Berkey et al.*, 1974; *McDiarmid et al.*, 1975; *Hardy et al.*, 1985]. In both the UV and the X-ray substorm we see eastward motion of the precipitation area, but the maximum in the morning sector is only seen in the X-ray substorm.

5. On the basis of the time development of X-ray fluxes in 2 hour local time sectors we have determined the location and time both for the substorm onset and the first enhanced X-ray fluxes seen in the morning sector, which can be related to the injection in the midnight sector. By using drift models of the gradient and curvature drift of electrons [*Lew*, 1961; *Roederer*, 1970], we have found the time delays to be consistent with drifting electrons in the energy range of 90-120 keV. On the basis of these results we believe that the maximum of precipitation observed in the morning sector is not caused by any new source region in the magnetosphere but rather to electrons injected close to midnight, drifting into the morning sector because of their gradient and curvature drift in the inhomogeneous magnetic field.

Appendix: Calculation of Drift Time for Electrons

A1. A Simple Method for Drift Time Calculation

A straightforward calculation of the energy, corresponding to the drift time, is given by (1) [*Lew*, 1961; *Hess*, 1968].

$$E = \frac{C}{Lt} \tag{1}$$

The L parameter is given in Earth radii, the energy E is given in MeV, and the time t is the time for the drift all around the Earth given in minutes. The constant C is 44 for equatorial mirroring electrons (pitch angles $=90°$) and 66 for precipitation electrons (pitch angles $<10°$). This formula is derived assuming local time independent drift velocity in a dipole magnetic field. In a dipole field the L value is a function of geomagnetic latitude λ and is given by (2).

$$L = \frac{1}{(\cos\lambda)^2} \tag{2}$$

For the September 12 event we found the onset of the maximum in the morning sector to occur 21.5 min and 9 sectors later than the substorm onset. The first maximum of the enhanced X-ray emission in the morning sector was delayed 34 min and 8 sectors relative to the first maximum in the onset region. These time delays correspond to 57 (102) min drift time around the Earth for the onsets (for the first maxima). Setting the onset location to be at 67° magnetic latitude, which is in the middle of 60° and 74° and in good agreement with Plates 1b and 1c we get L =6.6, which leaves us with the high energy of 115 keV (onsets) and a lower energy of 65 keV (first maxima). We have set the constant in (1) equal to 44 as we want to compare these results with a more advanced drift model, which is only valid for equatorial mirroring particles [*Roederer*, 1970]. However, by multiplying the calculated energies by a factor of 1.0-1.5 one gets the energies corresponding to precipitating electrons.

A2. A More Realistic Model of Drift Time Calculation

Neither during disturbed conditions nor during quiet times is the magnetic field at $L \geq 6.6$ dipole-like. At the dayside magnetosphere the solar wind causes compression of the field lines, which increases the magnetic strength but decreases the magnetic gradient. At the midnight magnetosphere the field lines are stretched because of tail currents, decreasing the magnetic strength but increasing the magnetic gradient. Analytically, the gradient and curvature drift velocity of electrons (and ions) is given by

$$V_D = \frac{\mathbf{B}}{qB^2} \times \left\{ -q\mathbf{E} + \frac{K}{B}(1 + (\cos\alpha)^2)\nabla\mathbf{B} \right\} \tag{3}$$

where $\mathbf{B}$ is the magnetic field, $\mathbf{E}$ is the electric field, q is the charge, K is the energy of the particle, and α is the pitch angle. From this formula we see that the assumption of constant drift velocity breaks down as the drift time strongly depends on the magnetic gradient, which is not constant along the drift path. The electron will drift faster on the nightside than on the dayside. This effect is probably reflected in the work of *Berkey et al.* [1974] as they found the velocities of the maximum absorption around onset in the midnight sector to be $\approx$2-3 times the velocities 30 min later in the late morning sector [see *Berkey et al.*, 1974, Figure 16].

The drift model of *Roederer* [1970] takes this azimuthal assymmerty into account by applying a cosine dependence of the drift velocity. By introducing the standoff distance R_{ST} the compression of the field lines and changes in the magnetic gradient is simulated. The standoff distance is defined as the point of equilibrium between the solar wind pressure and the Earth's magnetic field pressure. Taking into account the helium content of the solar wind, the standoff distance is given in Earth radii by (4) when n_{SW} is given in cm^{-3} and u_{SW} is given in km s^{-1} [*Walker and Russell*, 1995].

$$R_{ST} = 107.4(n_{sw}u_{sw}^2)^{-\frac{1}{6}} \tag{4}$$

Equatorially mirroring electrons tend to drift at contours of constant magnetic intensity, provided their energy is so high that we can ignore the electric field. According to *Roederer* [1970] the absolute value of the drift velocity for a particle drifting along the

$B = B_0$ = constant contour is given by

$$V_{B_0}(\varphi) \cong \overline{V} + \psi\cos\varphi \tag{5}$$

with

$$\overline{V} = \frac{3mv^2}{2q}\frac{1}{B_0}\left(\frac{B_0}{k_0}\right)^{1/3}\left(1 - \frac{4}{3}\frac{k_1}{B_0}\right) \tag{6}$$

$$\psi = \frac{5mv^2}{2q}\frac{k_2}{B_0^2} \tag{7}$$

where φ is the azimuthal position east of midnight, k_0 is a constant and k_1 and k_2 are both strongly dependent on the R_{ST}. The drift time can be calculated by:

$$\tau_D = \int_{\varphi_1}^{\varphi_2} \frac{r_{B_0}(\varphi)}{V_{B_0}(\varphi)}d\varphi \tag{8}$$

where φ_1 is the position of the onset and φ_2 is the position of the maximum of X-ray emission in the morning sector.

Applying this model, we have used B_0 = 100 nT, knowing that this is an upper limit of the field strength, as this value is obtained from a dipole field at 6.6 R_E. Mapping results of the substorm onset breakup area from the September 12 event using the Tsyganenko 96 model with input parameters from the Wind satellite gives a source region for the substorm onset of about 10-14 R_E. However, the models of *Roederer* [1970] and Tsyganenko are not consistent with each other. We therefore use the B_0 = 100 nT contour as an upper limit of the field strength, knowing that this gives us an upper limit of the calculated electron energy. The standoff distance for the September event is 10.3, and the calculated energies are 110 keV for the onsets and 65 keV for the first maxima. If a B_0 = 60 nT contour is used we get 95 and 55 keV.

References

Akasofu, S.-I., The development of the auroral substorm, *Planet. Space Sci.*, 12, 273–282, 1964.

Akasofu, S.-I., *Polar and Magnetospheric Substorms*, D. Reidel, Norwell, Mass., 1968.

Barcus, J. R., and T. J. Rosenberg, Energy spectrum for auroral-zone X rays, 1, Diurnal and type effects, *J. Geophys. Res.*, 71, 803–823, 1966.

Berger, M. J., and S. M. Seltzer, Bremsstrahlung in the atmosphere, *J. Atmos. Terr. Phys.*, 34, 85–108, 1972.

Berkey, F. T., V. M. Driatskij, K. Henriksen, B. Hultqvist, D. Jelly, T. I. Shchuka, A. Theander, and J. Yliniemi, A synoptic investigation of

particle precipitation dynamics for 60 substorms in IQSY(1964-65) and IASY(1969), *Planet. Space Sci.*, 22, 255–307, 1974.

Bjordal, J., H. Trefall, S. Ullaland, A. Bewersdorff, J. Kangas, P. Tanskanen, G. Kremser, K. H. Saeger, and H. Specht, On the morphology of auroral-zone X-ray events, I, Dynamics of midnight events, *J. Atmos. Terr. Phys.*, 33, 605–626, 1971.

Brice, N. M., and D. Lucas, Influence of magnetic convection and polar wind on loss of electrons from the outer radiation belt, *J. Geophys. Res.*, 76, 900–908, 1971.

Chenette, D. C., D. W. Datlowe, W. L. Imhof, T. L. Schumaker, and J. D. Tobin, Global spectroscopy and imaging of atmospheric X-ray bremsstrahlung: Instrumentation and initial results from the PEM/ AXIS instrument aboard the Upper Atmosphere Research Satellite, *Proc. SPIE Int. Soc. Opt. Eng.*, 1745, 16–25, 1992.

Elphinstone, R. D., J. S. Murphree, L. L. Cogger, D. Hearn, M. G. Henderson, and R. Lundin, Observations of changes to the auroral distribution prior to substorm onset, in *Magnetospheric Substorms, Geophys. Monogr. Ser.*, vol. 64, edited by J. R. Kan et al., pp. 257–275, AGU, Washington, D. C., 1991.

Elphinstone, R. D., J. S. Murphree, and L. L. Cogger, What is a global auroral substorm?, *Rev. Geophys.*, 34, 169–232, 1996.

Erickson, K. N., R. L. Swanson, R. J. Walker, and J. R. Winckler, A study of magnetospheric dynamics during auroral electrojet events by observation of energetic electron intensity changes at geosynchronous orbit, *J. Geophys. Res.*, 84, 931–942, 1979.

Fairfield, D. H., The average magnetic field configuration of the outer magnetosphere, *J. Geophys. Res.*, 73, 7329–7338, 1968.

Feldstein, Y. I., and G. V. Starkov, Dynamics of auroral belt and polar geomagnetic disturbances, *Planet. Space Sci.*, 15, 209, 1967.

Friedel, R., A. Korth, and G. Kremser, Substorm onsets observed by CRRES: Determination of energetic electron source regions, *J. Geophys. Res.*, 101, 13,137–13,154, 1996.

Germany, G. A., G. K. Parks, M. B. J. Cumnock, D. Lummerzheim, J. F. Spann, L. Chen, P. G. Richards, and F. J. Rich, Remote determination of auroral energy characteristics during substorm activity, *Geophys. Res. Lett.*, 24, 995–998, 1997.

Hardy, D. A., M. S. Gussenhoven, and E. Holeman, A statistical model of auroral electron precipitation, *J. Geophys. Res.*, 90, 4229–4248, 1985.

Hartz, T. H., and N. M. Brice, The general pattern of auroral particle precipitation, *Planet. Space Sci.*, 15, 301–329, 1967.

Hess, W. N., *The Radiation Belt and Magnetosphere*, Blaisdell, Waltham, Mass., 1968.

Imhof, W. L., J. R. Kilner, G. H. Nakano, and J. B. Reagan, Satellite X-ray mappings of sporadic auroral zone electron precipitation events in the local dusk sector, *J. Geophys. Res.*, 85, 3347–3359, 1980.

Imhof, W. L. et al., The Polar Ionospheric X-ray Imaging Experiment (PIXIE), *Space Sci. Rev.*, 71, 385–408, 1995.

Jelly, D., and N. Brice, Changes in Van Allen radiation associated with polar substorms, *J. Geophys. Res.*, 72, 5919–5931, 1967.

Jentsch, V., Electron precipitation in the morning sector of the auroral zone, *J. Geophys. Res.*, 81, 135–146, 1976.

Kangas, J., L. Lukkari, P. Tanskanen, H. Trefall, J. Stadsnes, G. Kremser, and W. Riedler, On the morphology of auroral-zone X-ray events, IV, Substorm-related electron precipitation in the local morning sector, *J. Atmos. Terr. Phys.*, 37, 1289–1303, 1975.

Lew, J. A., Drift rate in a dipole field, *J. Geophys. Res.*, 66, 2681–2685, 1961.

Liou, K., P. T. Newell, and C. I. Meng, Synoptic auroral distribution: A survey using polar ultraviolet imagery, *J. Geophys. Res.*, 102, 27,197–27,205, 1997.

McDiarmid, I. B., J. R. Burrows, and E. E. Budzinski, Average characteristics of magnetospheric electrons (140 eV to 200 keV) at 1400 kilometers, *J. Geophys. Res.*, 80, 73–79, 1975.

McPherron, R. L., Substorm related changes in the geomagnetic tail: The growth phase, *Planet. Space Sci.*, 20, 1521–1539, 1972.

Newell, P. T., and C.-I. Meng, Ionospheric projections of magnetospheric regions under low and high solar wind pressure conditions, *J. Geophys. Res.*, 99, 273–286, 1994.

Parks, G. K., F. V. Coroniti, R. L. McPherron, and K. A. Anderson, Studies of the magnetospheric substorms, 1, Characteristics of modulated energetic electron precipitation occurring during auroral substorms, *J. Geophys. Res.*, 73, 1685–1696, 1968.

Petrinec, S. M., J. Mobilia, D. Chenette, W. L. Imhof, and F. Fenrich, Statistical survey of auroral X-ray emissions: PIXIE observations, in *Proceedings of the International Conference on Substorms*, vol. 4, edited by Y. Kamide, Terra Sci., Tokyo, 1998.

Pytte, T., and H. Trefall, Auroral-zone electron precipitation events observed before and at the onset of negative magnetic bays, *J. Atmos. Terr. Phys.*, 34, 315–337, 1972.

Robinson, R. M., and R. R. Vondrak, Validation of techniques for space based remote sensing of auroral precipitation and its ionospheric effect., *Space Sci. Rev.*, 69, 331–407, 1994.

Robinson, R. M., G. T. Davidson, R. R. Vondrak, W. E. Francis, and M. Walt, A technique for interpretation of auroral bremsstrahlung X-ray spectra, *Planet. Space Sci.*, 37, 1053–1062, 1989.

Roederer, J. G., *Dynamics of Geomagnetically Trapped Radiation*, Springer Verlag, New York, 1970.

Rostoker, G., S.-I. Akasofu, J. Foster, R. A. Greenwald, Y. Kamide, K. Kawasaki, A. T. Y. Lui, R. McPherron, and C. T. Russell, Magnetospheric substorms: Definitions and signatures, *J. Geophys. Res.*, 85, 1663–1668, 1980.

Sandholt, P. E., C. J. Farrugia, J. Moen, O. Noraberg, B. Lybekk, T. Sten, and T. Hansen, A classification of dayside auroral forms and activities as a function of interplanetary magnetic field orientation, *J. Geophys. Res.*, 103, 23,325–23,345, 1998.

Sergeev, V. A., E. M. Sazhina, N. A. Tsyganenko, J. Å. Lundblad, and F. Søraas, Pitch angle scattering of energetic protons in the magnetotail current sheet as the dominant source of their isotropic precipitation into the nightside ionosphere, *Planet. Space Sci.*, 31, 1147–1155, 1983.

Sergeev, V. A., M. A. Shukhtina, R. Rasinkangas, A. Korth, G. D. Reeves, H. J. Singer, M. F. Thomsen, and L. I. Vagina, Event study of deep energetic particle injections during substorm, *J. Geophys. Res.*, 103, 9217–9234, 1998.

Sibeck, D. G., R. E. Lopez, and E. C. Roelof, Solar wind control of the magnetopause shape, location, and motion, *J. Geophys. Res.*, 96, 5489–5495, 1991.

Sletten, A., J. Stadsnes, and H. Trefall, Auroral-zone X-ray events and their relation to polar magnetic substorms, *J. Atmos. Terr. Phys.*, 33, 589–604, 1971.

Torr, M. R. et al., A far ultraviolet imager for the international solar-terrestrial physics mission., *Space Sci. Rev.*, 71, 329–383, 1995.

Vorobjev, V. G., G. V. Starkov, and Y. I. Feldstein, The auroral oval during the substorm development, *Planet. Space Sci.*, 24, 955–965, 1976.

Walker, R. J., and C. T. Russell, Solar-wind interactions with magnetized planets, in *Introduction to Space Physics*, edited by M. G. Kivelson and C. T. Russell, pp. 164–182, Cambridge Univ. Press, England, 1995.

Yeoman, T. K., M. P. Freeman, G. D. Reeves, M. Lester, and D. Orr, A comparison of midlatitude Pi2 pulsations and geostationary orbit particle injections as substorm indicators, *J. Geophys. Res.*, 99, 4085–4093, 1994.